

Light-induced microwave noise in superconducting microwave-optical transducers

Mingrui Xu^{✉,†}, Chunzhen Li^{✉,†}, Yuntao Xu, and Hong X. Tang^{✉,*}

Department of Electrical Engineering, Yale University, New Haven, Connecticut 06520, USA



(Received 15 September 2023; accepted 18 December 2023; published 12 January 2024)

Microwave-to-optical transducers are integral to the future of superconducting quantum computing, as they would enable scaling and long-distance communication of superconducting quantum processors through optical-fiber links. However, optically induced microwave noise poses a significant challenge in achieving quantum transduction between microwave and optical frequencies. In this work, we study light-induced microwave noise in an integrated electro-optical transducer harnessing the Pockels effect of thin-film lithium niobate. We reveal three sources of added noise with distinctive time constants ranging from sub-100 ns to milliseconds. Our results provide insights into the mechanisms and corresponding mitigation strategies for light-induced microwave noise in superconducting microwave-optical transducers and pave the way toward realizing the ultimate goal of quantum transduction.

DOI: [10.1103/PhysRevApplied.21.014022](https://doi.org/10.1103/PhysRevApplied.21.014022)

I. INTRODUCTION

The microwave-to-optical (MO) transducer will play an essential role in future quantum networks [1–4], where the quantum information will be processed by superconducting qubits [5,6] at microwave frequencies and transmitted using optical photons [7]. The added noise is a critical performance parameter for MO transducers, as any excessive noise would deteriorate the fidelity of the signal transduction. Typically, for a gigahertz electro-optical (EO) transducer [8,9] operating at low input powers, simple refrigeration of the device to temperatures in the tens of millikelvins range is sufficient to suppress thermal excitations in the microwave resonators. However, maintaining the microwave resonator at the ground state while retaining high transduction efficiency in the presence of a high-intensity optical drive is particularly challenging. Various schemes have been implemented to realize transduction at microwave ground state, including cavity EO [10,11], rare-earth-ion [12], and piezo-optomechanics [13,14] systems. However, the conversion efficiencies demonstrated thus far still fall significantly below unity. This fact hinders the realization of quantum state transduction, where an intense optical drive is critically required to achieve high conversion efficiency [15].

Recently, the pulsed optical drive has emerged as a promising approach to achieve higher conversion efficiency in various MO transduction schemes [10,13,14,16,17]. This technique allows for high-power optical drive and reduces overall heat dissipation at the

same time. Near-unity cooperativity has been achieved in a bulk lithium niobate EO platform, utilizing watt-scale pulses [16]. However, at millikelvin temperatures, where the cooling power is relatively weak, a strong optical drive applied to integrated transducers results in significant heating up of the device. This heat introduces additional microwave noise through photon absorption by dielectrics [18] and superconductors [19–22]. Therefore, there is a pressing need to gain a fundamental understanding of the mechanism underlying light-induced microwave noise in superconducting MO transducers. Such an understanding is crucial to explore potential strategies for noise suppression.

In this work, we study the microwave noise induced by a pulsed optical drive in an integrated superconducting-EO transducer. The transducer is implemented on a thin-film lithium niobate–(TFLN) niobium nitride (NbN) hybrid material platform as introduced in Ref. [23] and displayed in Fig. 1(a). Instead of investigating the microwave noise as a whole, which has been done in our previous work [10], three sources of noise have been identified here, including heating of the external thermal bath n_{bg} , fast-time-scale heating and cooling of an intrinsic thermal bath during the pulse rise-and-fall time $n_{i,fast}$, and slow-time-scale heating and cooling of the intrinsic thermal bath during the pulse-on and -off time $n_{i,slow}$. Moreover, the corresponding time constants for each noise source are measured and analyzed. n_{bg} has a relaxation time much longer than 5 ms, while that of $n_{i,fast}$ is much shorter than 100 ns. The time constant of $n_{i,slow}$ is more complicated, containing components ranging from 33 μ s to 6 ms. We also explore the dependence of light-induced microwave noise on the pulse peak power, the pulse width, and the pulse period. Both n_{bg} and $n_{i,slow}$

*hong.tang@yale.edu

[†]These authors contributed equally to this work.

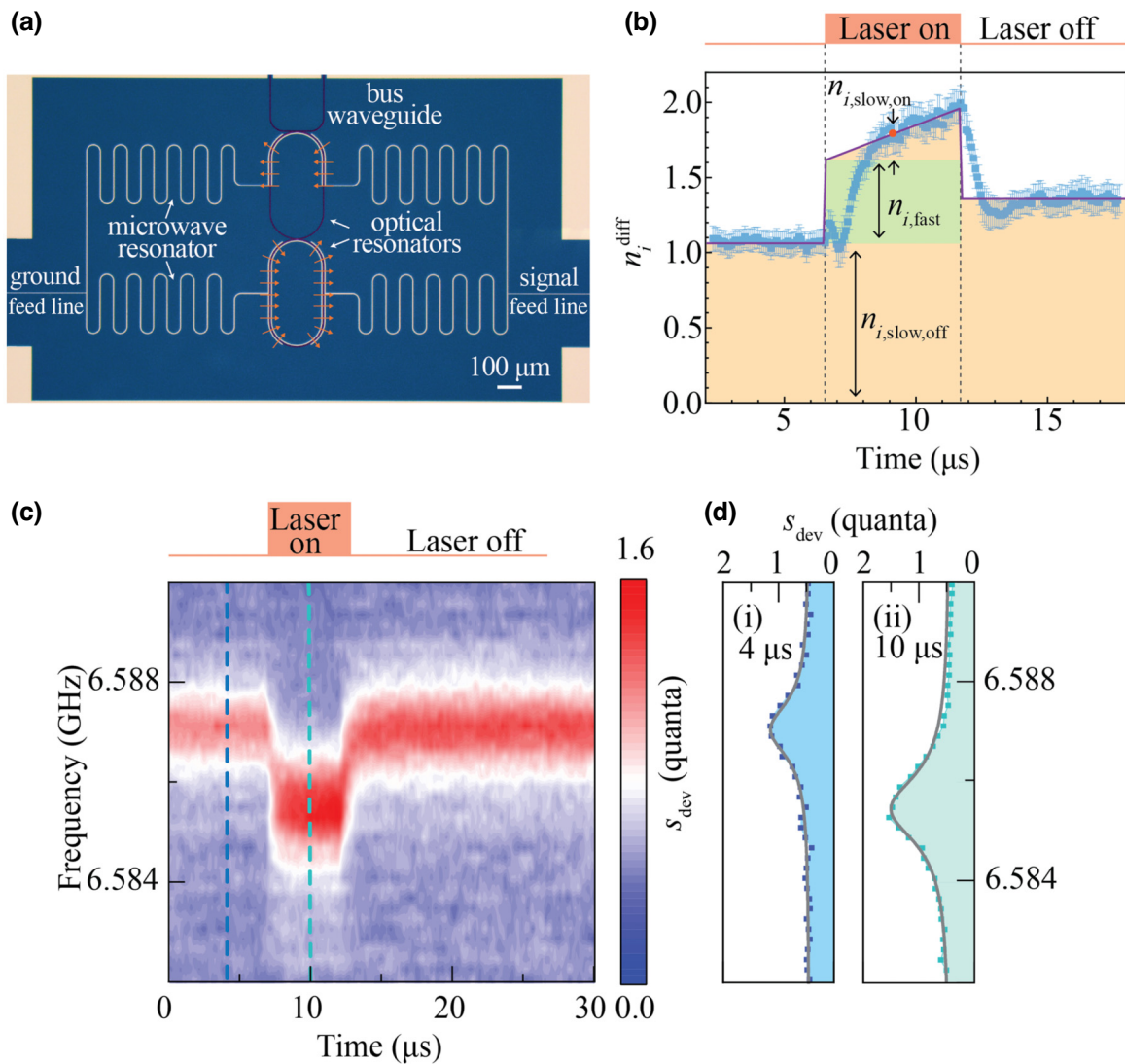


FIG. 1. (a) A false-colored microscopic image of the EO transducer. Two strongly coupled optical racetrack resonators are integrated with a superconducting microwave resonator. The microwave resonator is linked to a coplanar waveguide (CPW, not shown) for both rf coupling and dc biasing. The electrical field direction of the designed microwave mode is marked in the coupling regime. The figure is taken from Ref. [23]. (b) The temporal evolution of n_i^{diff} obtained at a pulse peak power of 6 dBm, a pulse width of 5 μs , and a pulse period of 1 ms. The optical drive is turned on and off at approximately 6.6 μs and 11.8 μs . The solid purple line is the extrapolation of n_i^{diff} . (c) The heat map shows the time evolution of the noise spectrum, with a pulse peak power of 5 dBm, a pulse width of 5 μs , and a pulse period of 1 ms. (d)(i) and (d)(ii) show snapshots of the power spectral density when the pulsed optical drive is on and off. The data in (d)(i) and (d)(ii) are cross sections of (c), marked in correspondingly colored dashed lines.

are related to the average power, while $n_{i,\text{fast}}$ can only be affected by the pulse peak power. These results suggest different noise-generation mechanisms in the system. Lastly, we discuss potential strategies to mitigate light-induced microwave noise and provide insights for the design of future integrated EO transducers, with the aim of further suppressing these detrimental noise effects.

II. METHOD

To investigate the dynamics of the thermal-bath temperatures during a pulsed optical drive, we employ

a calibration schedule as described in Appendix A to determine the input-line attenuation by using a variable temperature stage (VTS). We subsequently record the time evolution of the noise-power spectrum using an ultrahigh-frequency lock-in amplifier. This process involves two steps. First, we select a specific frequency and measure the noise power within a time window relative to the optical drive. We repeat this process numerous times and average the results to obtain a time trace. Second, we sweep the frequency and repeat the previous step for each frequency of interest. We alternate the measurement with the optical drive turning on and off. The difference between the data

of on-off experiments yields the excessive noise spectrum s_{dev} heat map [Fig. 1(c)] from the EO transducer.

The dynamic noise-measurement protocol outlined above requires precise knowledge of the state of the resonance, including the coupling rates and the resonant frequency, which can vary with time. We achieve this by probing the resonator with a weak coherent tone to monitor the time evolution of the resonance. This measurement is similar to acquiring a heat map of the noise power but instead of recording the noise power, we record the complex reflection of the resonator. By analyzing the reflection spectrum obtained at different time points, we can fit it to a Lorentzian function to extract the coupling rates and the resonant frequency accurately.

In measuring the time evolution of the noise spectrum, there is an important trade-off between the time resolution and the frequency resolution. On the one hand, studying the transition of optically induced microwave noise on the scale that is sub-100 ns is a challenging task. This is mainly due to two limiting factors: (a) the low-pass filter settling time of the lock-in amplifier; and (b) the rise-and-fall time of the pulsed drive (the acousto-optic modulator), which is on the scale of 35 ns. While factor (b) is fixed by our physical setup, we maximize the bandwidth for the low-pass filter in the lock-in amplifier, with a time constant of $t_c = 30$ ns, to record the noise spectrum with the best resolution, limited by our electronics as shown in Fig. 2(c).

On the other hand, while resolving the frequency envelope of the noise spectrum, we use $t_c = 1 \mu\text{s}$, which limits the temporal resolution to the microsecond scale. Figures 1(c) and 1(d) present an example. As shown in Figs. 1(c) and 1(d), a consistent background noise of 0.55 quanta is observed over the frequency range of interest. In the pulse-off period [Fig. 1(d)(i)], there is a resonant peak at 6.587 GHz associated with finite thermal excitation. When the pulse is on [Fig. 1(d)(ii)], this resonance down shifts by 1.5 MHz and the resonant line-width broadens. At the new resonant frequency, there is stronger thermal excitation. The thermal-bath occupancy can be extracted by applying the model described in Appendix B, where n_{bg} and n_i^{diff} are the only free parameters. In Sec. III, the dynamics of both will be investigated.

III. RESULTS

A. Dynamics of n_{bg}

We first examine n_{bg} , which combines the thermal excitation due to the external thermal bath of the superconducting resonator and the added noise from the output readout line. By analyzing the heat map shown in Fig. 1(c), which captures the evolution of the noise-power spectrum over time, it becomes evident that n_{bg} remains constant over time on the scale of microseconds and exhibits no discernible frequency dependence within the 10-MHz span.

Figure 2(a) illustrates the dynamics of n_{bg} . The data points are collected while the optical drive is on and off and the different traces correspond to different optical-drive peak powers. It is evident that in all these traces, n_{bg} does not change with regard to the status of the optical drive being on or off. Due to the finite time constant ($1 \mu\text{s}$) of the filter in our measurement electronics, the noise spectrum is artificially distorted right after the rise-and-fall edges of the optical drive. These small artificial bumps can be observed in the orange trace.

To investigate n_{bg} on a longer time scale, we characterize its relaxation between optical-drive pulses with a period of 5 ms, as shown in Fig. 2(a) inset. In comparison to the dashed horizontal lines provided as visual guides, we find that n_{bg} does not change significantly within the millisecond time scale, indicating that n_{bg} likely has a relaxation time much longer than 5 ms. These observations rule out the possibility of n_{bg} being caused by leaked infrared light impacting superconducting components, such as Josephson traveling-wave parametric amplifiers (JTWPAs), in the cryogenic microwave circuits. Otherwise, we would observe more changes in n_{bg} while the optical drive is turned on and off. Instead, the results suggest that the heating of the dilution refrigerator might be the cause of the excessive n_{bg} .

To gain further understanding of the source of n_{bg} , we characterize the dependence of n_{bg} on the average drive power ($P_{\text{avg}} = P_{\text{peak}} \times \text{duty cycle}$) in Fig. 3(a). This plot aggregates three sets of measurement results where we sweep the pulsed drive peak power, the pulse width, or the pulse period. By fitting all data to an exponential growth function (dashed red line), we find that $n_{\text{bg}} \approx P_{\text{avg}}^{0.82}$. The fact that all data points from three different measurement configurations coalesce very well also indicates that n_{bg} is only affected by the average optical-drive power. These results confirm that n_{bg} is a result of the heating of the dilution refrigerator.

B. Dynamics of n_i^{diff}

1. “Fast”- and “slow”-responding noise components

In marked contrast to n_{bg} , which seems to have a very long relaxation time and does not respond to different illumination conditions, the dynamics of n_i^{diff} exhibits a significantly richer behavior across various time scales. In order to further understand the mechanisms of these noise components, we separate n_i^{diff} into three components:

$$n_i^{\text{diff}} = n_{i,\text{fast}} + n_{i,\text{slow,off}} + n_{i,\text{slow,on}}. \quad (1)$$

This division is also illustrated in Fig. 1(b), where an example time trace of n_i^{diff} is presented. To account for the slow transition slope masked by the low-pass filter, we extrapolate the data (solid purple line) based on the linear fit of steady measurement results.

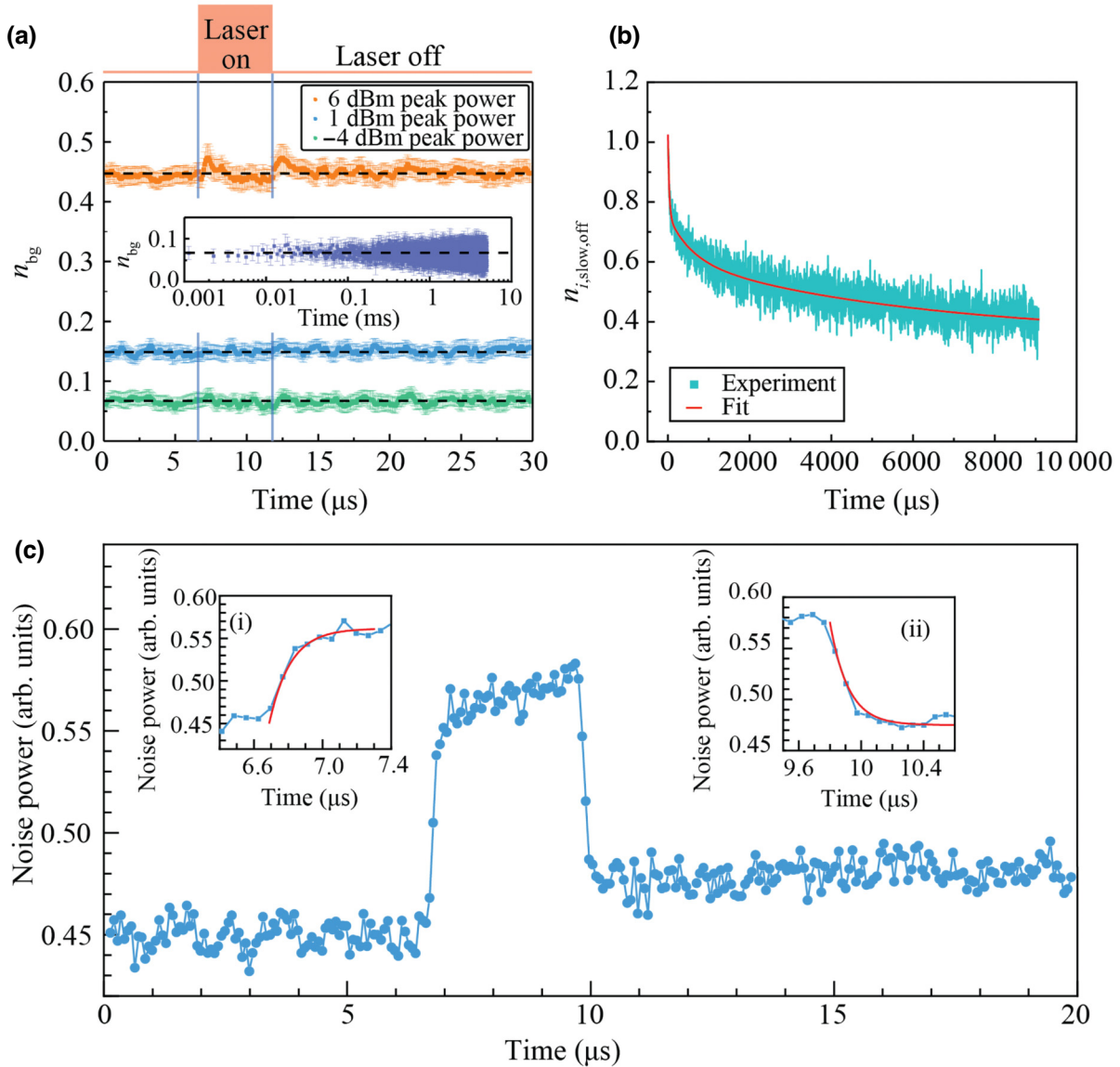


FIG. 2. (a) The dynamics of n_{bg} over 30 μ s, where the optical drive is turned on and off at approximately 6.6 μ s and 11.8 μ s as marked. The pulsed drive is configured with different peak powers and the same duty cycle of 0.5%. The inset shows the dynamics of n_{bg} over a time span of 5 ms after the optical drive is turned off. The pulsed drive is configured with a peak power of 0 dBm and a pulse width of 10 μ s. The black dashed lines are all horizontal lines as guide to the eye. (b) Time traces of $n_{i,slow,off}$ while the peak power is 0 dBm, the pulse width is 10 μ s, and the pulse period is 10 ms. The cyan trace is the experimental data, while the red trace is the fit. (c) The output-noise-power time dynamics with $t_c = 30$ ns. Insets (i) and (ii) are enlarged views of the rise-and-fall edges of (c), where fits to exponential functions are shown in the red curves.

As shown in Fig. 1(b), we define $n_{i,fast}$ as the “fast-responding” part of n_i^{diff} . It is obtained from the time-evolution traces of n_i^{diff} as $n_{i,fast} = n_i^{\text{diff}}|_{\text{after laser}} - n_{i,slow,off}$. Here, $n_i^{\text{diff}}|_{\text{after laser}}$ is defined as n_i^{diff} at the moment immediately after the optical drive is turned on. By assuming a linear change in n_i^{diff} when the optical drive is on, we extrapolate $n_i^{\text{diff}}|_{\text{after laser}}$ from the steady-state measurement results. The time when the optical drive is turned on and off are determined by the moment when the resonant

frequency shifts in the coherent measurement with $\tau_c = 30$ ns.

The other two noise components are the “slow-responding” part of n_i^{diff} : $n_{i,slow,off}$ is defined as the n_i^{diff} right before the optical drive is on, while $n_{i,slow,on}$ is the build-up of n_i^{diff} during the pulse-on period. Given the narrow optical-drive pulse width, it is reasonable to assume that the increase of n_i^{diff} is linear after the optical drive is turned on and that this is the basis for the linear extrapolation

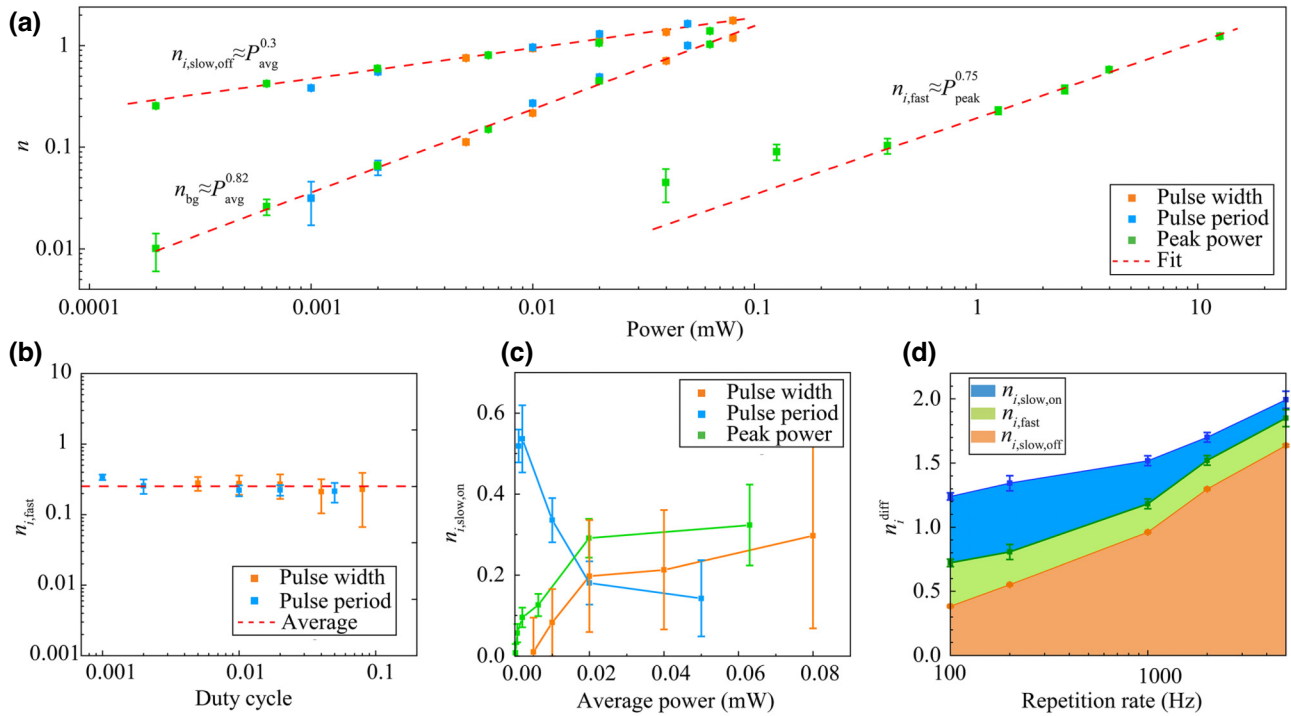


FIG. 3. (a) n_{bg} and $n_{i,slow,off}$ as a function of the average power of the optical drive and $n_{i,fast}$ as a function of the pulse peak power of the optical drive. The orange data points correspond to optical drives with a 0-dBm peak power and a 1-ms pulse period, while the pulse width is swept from 5 μ s to 80 μ s. The blue data points correspond to optical drives with a 0-dBm peak power and a 10- μ s pulse width, while the pulse period is swept from 0.2 ms to 10 ms. The green data points correspond to optical drives with a 5- μ s pulse width and a 1-ms pulse period, while the pulse peak power is swept from -14 dBm to 11 dBm. The dashed red line is an exponential fit to all the data. The fits show $n_{bg} \approx P_{avg}^{0.82}$ and $n_{i,slow,off} \approx P_{avg}^{0.3}$ and $n_{i,fast} \approx P_{peak}^{0.75}$. (b) The dependence of $n_{i,fast}$ on the duty cycle of the optical drives. The orange and blue data points correspond to the same pulse configurations as in (a). The red dashed line is the average value of the data. (c) $n_{i,slow,on}$ as a function of the average power of the optical drive. The solid lines are used as visual guides. (d) The dependence of n_i^{diff} and its different components on the repetition rate of the optical drives. The pulse peak power is fixed at 0 dBm, the pulse width is 10 μ s, and the repetition rate is swept from 100 Hz to 5000 Hz.

to obtain n_i^{diff} during the pulse-on period. We use n_i^{diff} at the middle point of the optical-drive pulse to indicate the average intrinsic thermal-bath temperature. Therefore, we define $n_{i,slow,on} = n_i^{\text{diff}}|_{\text{midpulse}} - n_i^{\text{diff}}|_{\text{afterlaser}}$.

2. “Fast”-light-induced microwave noise generation

In Fig. 2(c), we show the dynamics of n_i^{diff} from a high-time-resolution measurement. Because of the small time constant, the noise-power-measurement bandwidth is much larger than the resonance line width, making it difficult to accurately extract the occupancy of the different thermal baths. Therefore, we present the output noise power as an indication of the changes of n_i^{diff} . The fits to the rise-and-fall edges as shown in Figs. 2(c)(i) and 2(c)(ii) consistently show a relaxation time of $120 \text{ ns} \pm 30 \text{ ns}$, which is mainly limited by the pulse rise-and-fall time. The actual transition should be much faster than 120 ns.

To determine the dependence of $n_{i,fast}$ on the optical-drive power, we first sweep the pulse peak power while fixing the pulse width and the pulse period at 5 μ s and

1 ms. The results are shown in Fig. 3(a), where we find that $n_{i,fast}$ increases as $P_{peak}^{0.75}$. In order to maintain $n_{i,fast}$ below 0.1, P_{peak} needs to be set below 0.3 mW, while the threshold for $n_{i,fast} = 1$ is $P_{peak} = 10 \text{ mW}$. Then, we investigate the dependence of $n_{i,fast}$ on the pulse width and the pulse period, respectively. The results in Fig. 3(b) show that $n_{i,fast}$ does not change significantly with different pulse configurations as long as the pulse peak power is constant. Deviations from the average value as shown by the dashed red line could be a result of different device temperatures, as a higher duty cycle leads to more average power dissipation and a higher local temperature of the device and vice versa.

This fast-light-induced microwave noise could be attributed to light absorption by the superconductor [19–22]. It can be understood as the same mechanism as for superconducting single-photon detectors. When optical photons are directly absorbed by the superconductor, quasiparticles are generated in an energy down-conversion process. In materials such as NbN, this process could be much faster than 1 ns. The other possible mechanism is

the local heating due to optical photons being absorbed by the optical waveguide and the surrounding substrate materials next to the superconducting resonator [18]. These two mechanisms cannot be distinguished in our experiment.

3. “Slow”-light-induced microwave noise generation

In Fig. 2(b), we show the time evolution of $n_{i,\text{slow},\text{off}}$ up to 9 ms. We fit the decay curve to a triple-exponential decay model: $n_{i,\text{slow},\text{off}} = n_1 e^{(-t/\tau_1)} + n_2 e^{(-t/\tau_2)} + n_3 e^{(-t/\tau_3)} + n_4$. The data and the fit are shown in cyan and red traces, respectively. Three different time constants, $\tau_1 = 33 \pm 6 \mu\text{s}$, $\tau_2 = 0.6 \pm 0.1 \text{ ms}$, and $\tau_3 = 6 \pm 1 \text{ ms}$, are extracted. Additionally, the fit shows a constant background of $n_4 = 0.36$, indicating that there is still a significant portion of $n_{i,\text{slow},\text{off}}$ that decays at a time scale that is much longer than 9 ms. For a typical pulsed measurement with repetition on the order of the kilohertz range, this results in a build-up of thermal fluctuation in the EO transducer that accumulates through the pulse sequences.

If we take a look at the optical power dependence of $n_{i,\text{slow},\text{off}}$ as shown in Fig. 3(a), all the data show a similar trend, which is represented by the dashed line as $n_{i,\text{slow},\text{off}} \propto P_{\text{avg}}^{0.3}$. This trend could be explained by the increased material heat conductivity with higher temperature at cryogenic temperatures. Specifically, we know that at the low-temperature limit, the thermal conductivity of lithium niobate (LN) and sapphire increases as the cube of the temperature and that of copper increases proportionally to the temperature. We consider a simple model comprised of a point heater (an optical waveguide) thermalized to a large thermal reservoir (a dilution refrigerator) through a solid media. Assuming that the thermal conductivity of the solid media is dominated by phonons and follows a cubic law with regard to the temperature, the equilibrium temperature of the heater would be proportional to the temperature to the power of 1/4. In our experiment, the power-law relation between the temperature and the average optical power dissipation has a factor of 0.3, suggesting that the source of $n_{i,\text{slow},\text{off}}$ could be attributed to the heating-up of the device and the copper package, while LN and sapphire might play a more dominant role in thermalizing the intrinsic thermal bath associated with $n_{i,\text{slow},\text{off}}$.

We also investigate the optical power dependence of $n_{i,\text{slow},\text{on}}$. In contrast to the behavior of $n_{i,\text{slow},\text{off}}$, the data in Fig. 3(c) exhibit distinctive trends. As the peak power and pulse width of the optical drive are varied to increase the average power, $n_{i,\text{slow},\text{off}}$ shows an upward trend. This difference in optical power dependence could be attributed to the local heating of the device chip and the package under different pulse configurations. Interestingly, $n_{i,\text{slow},\text{off}}$ experiences a decline as the average power of the optical drive increases when the optical-drive pulse period is varied.

This could be explained by the reduced thermal conductivity in materials at lower cryogenic temperatures, leading to a more rapid temperature increase.

How effective is decreasing the repetition rate in suppressing n_i^{diff} ? The answer can be found in Fig. 3(d). Here, we fix the pulsed peak power at 0 dBm and the pulse width at 10 μs , while sweeping the pulse repetition rate from 5000 Hz to 100 Hz. The data show that as the repetition rate decreases, $n_{i,\text{slow},\text{off}}$ decreases with the average heat dissipation while $n_{i,\text{slow},\text{on}}$ increases with lower repetition, despite the same power and duration of each optical-drive pulse. On the other hand, $n_{i,\text{fast}}$ does not change significantly with the repetition. Therefore, although reducing the repetition rate of optical-drive pulses could suppress light-induced microwave noise, its effectiveness is limited by the fast-responding noise $n_{i,\text{fast}}$ and the build-up of thermal noise while the optical drive is on $n_{i,\text{slow},\text{on}}$. As a result, the power-handling capability of on-chip EO transducers should be boosted by improving the design of the chip and the packaging.

IV. DISCUSSION AND CONCLUSIONS

This study reveals that the light-induced microwave noise is dominated by the dissipation of optical power in the EO transducer system and scattered photons shining on the superconductor. We argue that efficient fiber-chip interfaces, efficient light shielding, and superfluid helium immersion could be the key to mitigating these sources of microwave noise.

First, an efficient fiber-chip interface could reduce the amount of optical power dissipating in the device package. Considering the efficiency of photons passing from the input fiber to the on-chip waveguide as η_{in} and that of photons passing from the waveguide to the output fiber as η_{out} , the transmission amplitude of the optical cavity is T . Assuming that the optical power in the waveguide before the optical cavity is P_t , then the power sent to the input fiber is $P_{\text{in}} = P_t / \eta_{\text{in}}$. For simplicity, we do not consider the optical power dissipating in the straight waveguide, as the loss is usually much smaller (0.03 dB/cm for TFLN waveguides) than the extinction of optical resonances. We can then derive the total amount of power dissipated in the system as

$$P_{\text{heat}} = P_t \left[\frac{1}{\eta_{\text{in}}} - 1 + |T|^2 (1 - \eta_{\text{out}}) \right]. \quad (2)$$

This equation highlights the important role that η_{in} and η_{out} play in heat dissipation. Improving the fiber-to-chip efficiency from 50% to 80% can reduce the heat dissipation from the optical drive by 75% at most. Additionally, designing the optical resonances in the over-coupled or under-coupled regimes can lead to a larger T , resulting in more optical photons dissipating in the system through the external decay of the optical cavity.

Second, to address scattered light shining on the superconducting resonator, several design strategies can be employed. One approach is to use metal shields to block the direct propagation of photons in the substrate and the vacuum toward the superconducting resonator. For grating couplers, coating the backside of the grating coupler with metal can redirect light away from the superconducting resonator. In flip-chip-bonded EO devices, coating the photonic chip with metal can shield stray light in the photonic chip substrate from shining on the inductor of the superconducting resonator. Additionally, using metal such as gold as light shields can also enhance the thermal conductivity between the device chip and the copper device packaging, helping to dissipate heat.

Finally, immersing the device in superfluid helium can greatly increase the heat dissipation rate for the device [24,25], due to the exceptional heat-transport properties of superfluid helium. This approach can effectively suppress microwave noise induced by local heating [26–28]. However, it does have two limitations. First, the total amount of heat dissipation is still limited by the cooling power of the dilution refrigerator. For example, an average optical-drive power of -6 dBm ($250\ \mu\text{W}$) will inevitably heat up the mixing chamber to $100\ \text{mK}$, resulting in additional thermal noise. Second, for any microwave noise generated through superconductor absorption of photons, superfluid helium is unlikely to be effective. Nonetheless, superfluid helium immersion would provide valuable high-capacity cooling to allow the device to operate at ground state with higher drive powers and would provide additional insights into the sources of light-induced microwave noises.

In conclusion, we present a study of added noise in an on-chip integrated EO transducer. We examine different sources of microwave noise, including both external and intrinsic baths. We discover that the external-bath temperature increase is largely determined by the average optical-drive power dissipation, while the intrinsic bath is composed of various components with distinct relaxation times, ranging from submicroseconds to beyond milliseconds. We analyze the dependencies of each noise source and provide an understanding of potential noise-generation mechanisms. Finally, we discuss various noise-mitigation strategies for different noise sources. These insights can guide the design of future EO transducers for increasing power-handling capability, making quantum transduction feasible.

ACKNOWLEDGMENTS

We acknowledge funding support from the U.S. Department of Energy (DOE) Office of Science, National Quantum Information Science Research Centers, Co-design Center for Quantum Advantage (C2QA), under Contract No. DE-SC0012704. H.X.T. acknowledges partial funding support from the through the Engineering Research Center

(ERC) Center for Quantum Networks (CQN), under Grant No. EEC-1941583, and early support from the Army Research Office on the quantum transducer development (through Grant No. W911NF-18-1-0020). The JTWPAs used in this experiment are provided by the Intelligence Advanced Research Projects Activity (IARPA) and the Massachusetts Institute of Technology (MIT) Lincoln Laboratory. We would like to thank Dr. Yong Sun, Dr. Lauren McCabe, Mr. Kelly Woods, and Dr. Michael Rooks for assistance in device fabrication.

APPENDIX A: OUTPUT-LINE CALIBRATION PROTOCOL

Calibration of the gain and added noise of the output line is crucial for accurate determination of the absolute value of the light-induced noise in the device under test (DUT). The output-line calibration is performed by sourcing the DUT with a VTS in the mixing chamber of the dilution refrigerator, the thermal occupation of which follows a Bose-Einstein distribution: $n_{\text{VTS}} = 1/(\exp(hf/k_B T_{\text{VTS}}) - 1)$. The noise-power spectral density is then measured at the output of the dilution refrigerator using a spectrum analyzer or lock-in amplifier, after the amplification chain featuring a JTWPAs.

The noise-power spectrum P is thus linked to the VTS output through

$$P = BW \times G_{\text{sys}}(n_{\text{VTS},s}\hbar\omega_s + n_{\text{VTS},i}\hbar\omega_i + n_q\hbar\omega_s + n_{\text{sys}}\hbar\omega_s). \quad (\text{A1})$$

In this equation, BW represents the measurement resolution bandwidth, while $n_{\text{VTS},s}$ and $n_{\text{VTS},i}$ are the thermal photon numbers of the VTS output at the signal frequency ω_s and idler frequency ω_i of the amplifier, respectively. G_{sys} and n_{sys} are the gain and the added noise of the output line referred to the VTS, separately. $n_q = 1/2$ represents the quantum fluctuations. Note that here we assume that the gain of the parametric amplifier is very large. Otherwise, the gain coefficients for $n_{\text{VTS},s}$ and $n_{\text{VTS},i}$ will be different.

To determine G_{sys} and n_{sys} , we first detune the microwave resonance from the frequencies of interest, so that the device does not contribute to the calibration of G_{sys} . After that, we sweep the temperature of VTS to obtain G_{sys} and n_{sys} as a function of frequency and then fit the data to Eq. (A1). Given the calibrated gain results, we can also determine the attenuation of the input line to the VTS output plane by subtracting the output-line gain from the total transmission of the setup characterized with a vector-network analyzer.

Due to the small attenuation between VTS and the device, the characterized device noise presented in this work should always be slightly overestimated compared to the actual device noise.

APPENDIX B: MICROWAVE THERMAL-BATH TEMPERATURE EXTRACTION

To understand the microwave noise generated by optical drives in electronic optical transducers, we need to analyze the sources of noise in these devices. To accomplish this, we measure the temperature of the thermal bath that is connected to the microwave resonator through intrinsic and extrinsic channels, as illustrated in Fig. 4(a). These thermal-bath temperatures represent a universal value that can be applied to other integrated EO devices with similar physical characteristics, as they are not influenced by the extraction ratio or electro-optical coupling. By studying the thermal-bath temperature, we can gain a quantitative understanding of the optically induced microwave noise that can be referenced by different EO transducers, despite differences in their extraction ratio or conversion efficiency.

To measure the excessive microwave output noise, we perform an on-off characterization. First, we make sure that the external magnetic field is turned off, which allows the microwave resonator to stay at its original frequency. Then, we apply the optical drive, to induce excessive noise that is coupled to the microwave transmission line and the superconducting resonator. Therefore, the output-noise-power spectrum becomes

$$P = BW \times G_{\text{sys}} \hbar \omega_s (n_q + n_{\text{sys}} + \Delta n_{\text{sys}}) + BW \times G_{\text{dev}} \hbar \omega_s s_{\text{out}}. \quad (\text{B1})$$

Here, $G_{\text{dev}} = LG_{\text{sys}}$ and L is the attenuation between the VTS and the EO transducer. Note that Eq. (B1) and the following analysis are only valid when the cooperativity is much smaller than 1. Otherwise, we would need to take the

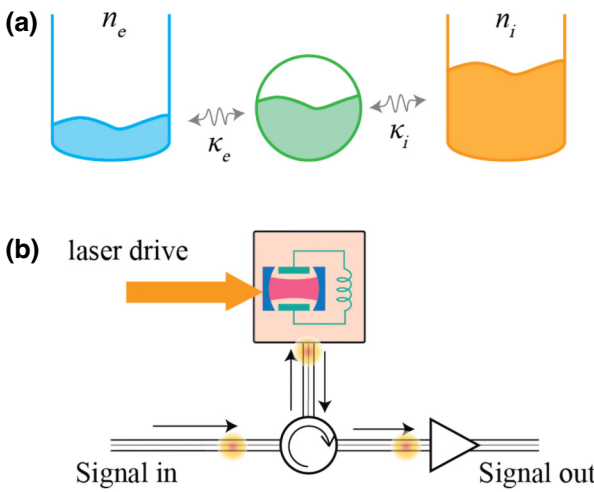


FIG. 4. (a) A diagram of the superconducting mode being thermalized through the intrinsic and external coupling channels. (b) The possible locations where the light-induced excessive noise couples to the system.

loss through the electro-optical effect into account. According to our previous experiment with a similar configuration [10], the attenuation $L = 91\% \pm 4\%$. Thus G_{VTS} can be used as a good estimate of G_{dev} to an accuracy of 10%. It is worth noting that because of this systematic error, the characterized device noise presented in the work should be slightly overestimated compared to the actual device noise. By means of the approximation $L = 1$, we can simplify the equation to

$$P = BW \times G_{\text{sys}} \hbar \omega_s (n_q + n_{\text{sys}} + \Delta n_{\text{sys}} + s_{\text{out}}). \quad (\text{B2})$$

The term Δn_{sys} represents the potential increase in the output-chain added noise after the EO transducer when the optical drive is on, which is referred back to the input of the EO transducer [see Fig. 4(b)], and s_{out} represents the power spectral density at the output of the EO transducer as

$$s_{\text{out}} = a_{\text{out}}^\dagger a_{\text{out}} = \mathcal{R}(\omega) n_e + \mathcal{T}(\omega) n_i, \quad (\text{B3})$$

where $\mathcal{T}(\omega) = \kappa_i \kappa_e / ((\kappa/2)^2 + (\omega - \omega_0)^2)$ and $\mathcal{R}(\omega) = 1 - \mathcal{T}(\omega)$. ω_0 , κ_e , and κ_i are the angular resonant frequency, the external coupling rate, and the intrinsic coupling rate of the superconducting resonator, respectively. n_i and n_e each denote the power spectral density of the fields that are coupled to the resonator through the intrinsic and external coupling channels, separately.

Combining Eqs. (B2) and (B3), we arrive at

$$P = BW \times G_{\text{sys}} \hbar \omega_s [n_q + n_{\text{sys}} + \Delta n_{\text{sys}} + n_e + \mathcal{T}(\omega)(n_i - n_e)]. \quad (\text{B4})$$

Since in this part of the experiment, we maintain VTS at the base temperature, usually 60 mK, its contribution to the input field of the superconducting resonator is negligible. Therefore, when the optical drive is off, we can assume that $n_e = 0$. Additionally, when the optical drive is off, it can be assumed that the device is thermalized to the dilution refrigerator base temperature, which is usually set to 50 mK for a better cooling power. In this case, we can also assume that $n_i = 0$. Therefore, when the optical drive is off, the output noise spectrum can be expressed as

$$P_{\text{off}} = BW \times G_{\text{sys}} \hbar \omega_s (n_q + n_{\text{sys}}). \quad (\text{B5})$$

In order to extract the light-induced microwave noise, we measure the P_{on} spectrum when the optical drive is on, followed by a measurement of P_{off} . It is important to maintain the same gain of the output chain during the on-off measurement. Then, we can extract the excess noise spectrum through

$$s_{\text{dev}} = (P_{\text{on}} - P_{\text{off}}) / (BW \times G_{\text{sys}} \hbar \omega_s) \quad (\text{B6})$$

$$= \Delta n_{\text{sys}} + n_e + \mathcal{T}(\omega)(n_i - n_e), \quad (\text{B7})$$

with knowledge of the intrinsic and external coupling rates and therefore of $\mathcal{T}(\omega)$. Note that here we do not have the

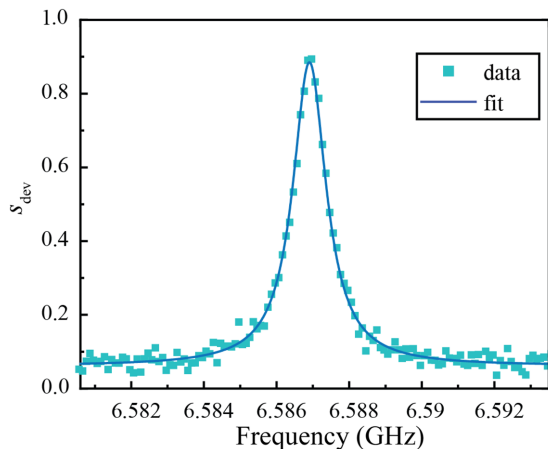


FIG. 5. The experimental data of s_{dev} and its fit.

ability to separate the optically induced noise coupled to the microwave transmission lines before and after the system, which is n_e and Δn_{sys} , respectively. Therefore, we cannot determine the absolute value of n_e and n_i . Instead, we shall focus on the two parameters that can be extracted experimentally:

$$n_{\text{bg}} = \Delta n_{\text{sys}} + n_e, \quad (\text{B8})$$

$$n_i^{\text{diff}} = n_i - n_e. \quad (\text{B9})$$

These experimental variables will set the limits for the thermal-bath occupancy as

$$0 < n_e < n_{\text{bg}}, \quad (\text{B10})$$

$$n_i^{\text{diff}} < n_i < n_i^{\text{diff}} + n_{\text{bg}}. \quad (\text{B11})$$

In Fig. 5, we show an example of the s_{dev} curve and its fit. The model that we use to fit the data is

$$s_{\text{dev}} = n_{\text{bg}} + \mathcal{T}(\omega)n_i^{\text{diff}}. \quad (\text{B12})$$

In this model, the only free parameters are n_{bg} and n_i^{diff} , while the resonance frequency and coupling rates on which $\mathcal{T}(\omega)$ is dependent are extracted from coherent reflection characterization of the microwave resonator. Since the cooperativity in these devices that we study is much smaller than 1, we can ignore the broadening of the line width of the microwave resonator when the optical drive is on.

Proposal for heralded generation and detection of entangled microwave-optical-photon pairs, *Phys. Rev. Lett.* **124**, 010511 (2020).

- [3] L. Jiang, J. M. Taylor, A. S. Sørensen, and M. D. Lukin, Distributed quantum computation based on small quantum registers, *Phys. Rev. A* **76**, 062323 (2007).
- [4] J. I. Cirac, P. Zoller, H. J. Kimble, and H. Mabuchi, Quantum state transfer and entanglement distribution among distant nodes in a quantum network, *Phys. Rev. Lett.* **78**, 3221 (1997).
- [5] J. Clarke and F. K. Wilhelm, Superconducting quantum bits, *Nature* **453**, 1031 (2008).
- [6] M. H. Devoret and R. J. Schoelkopf, Superconducting circuits for quantum information: An outlook, *Science* **339**, 1169 (2013).
- [7] J. L. O'Brien, A. Furusawa, and J. Vučković, Photonic quantum technologies, *Nat. Photonics* **3**, 687 (2009).
- [8] M. Tsang, Cavity quantum electro-optics, *Phys. Rev. A* **81**, 063837 (2010).
- [9] M. Tsang, Cavity quantum electro-optics. II. Input-output relations between traveling optical and microwave fields, *Phys. Rev. A* **84**, 043845 (2011).
- [10] W. Fu, M. Xu, X. Liu, C.-L. Zou, C. Zhong, X. Han, M. Shen, Y. Xu, R. Cheng, S. Wang, L. Jiang, and H. X. Tang, Cavity electro-optic circuit for microwave-to-optical conversion in the quantum ground state, *Phys. Rev. A* **103**, 053504 (2021).
- [11] W. Hease, A. Rueda, R. Sahu, M. Wulf, G. Arnold, H. G. L. Schwefel, and J. M. Fink, Bidirectional electro-optic wavelength conversion in the quantum ground state, *PRX Quantum* **1**, 020315 (2020).
- [12] J. Rochman, T. Xie, J. G. Bartholomew, K. Schwab, and A. Faraon, Microwave-to-optical transduction with erbium ions coupled to planar photonic and superconducting resonators, *Nat. Commun.* **14**, 1153 (2023).
- [13] M. Mirhosseini, A. Sipahigil, M. Kalaei, and O. Painter, Superconducting qubit to optical photon transduction, *Nature* **588**, 599 (2020).
- [14] M. Forsch, R. Stockill, A. Wallucks, I. Marinković, C. Gärtner, R. A. Norte, F. van Otten, A. Fiore, K. Srinivasan, and S. Gröblacher, Microwave-to-optics conversion using a mechanical oscillator in its quantum ground state, *Nat. Phys.* **16**, 69 (2020).
- [15] E. Zeuthen, A. Schliesser, A. S. Sørensen, and J. M. Taylor, Figures of merit for quantum transducers, *Quantum Sci. Technol.* **5**, 034009 (2020).
- [16] R. Sahu, W. Hease, A. Rueda, G. Arnold, L. Qiu, and J. M. Fink, Quantum-enabled operation of a microwave-optical interface, *Nat. Commun.* **13**, 1276 (2022).
- [17] X. Han, W. Fu, C. Zhong, C.-L. Zou, Y. Xu, A. A. Sayem, M. Xu, S. Wang, R. Cheng, L. Jiang, and H. X. Tang, Cavity piezo-mechanics for superconducting-nanophotonic quantum interface, *Nat. Commun.* **11**, 3237 (2020).
- [18] S. Mobassem, N. J. Lambert, A. Rueda, J. M. Fink, G. Leuchs, and H. G. Schwefel, Thermal noise in electro-optic devices at cryogenic temperatures, *Quantum Sci. Technol.* **6**, 045005 (2021).
- [19] K. Il'in, M. Lindgren, M. Currie, A. Semenov, G. Gol'Tsman, R. Sobolewski, S. Cherednichenko, and E. Gershenson, Picosecond hot-electron energy relaxation in

- nbn superconducting photodetectors, *Appl. Phys. Lett.* **76**, 2752 (2000).
- [20] P. K. Day, H. G. LeDuc, B. A. Mazin, A. Vayonakis, and J. Zmuidzinas, A broadband superconducting detector suitable for use in large arrays, *Nature* **425**, 817 (2003).
- [21] M. Beck, M. Klammer, S. Lang, P. Leiderer, V. V. Kabanov, G. N. Gol'Tsman, and J. Demsar, Energy-gap dynamics of superconducting NbN thin films studied by time-resolved terahertz spectroscopy, *Phys. Rev. Lett.* **107**, 177007 (2011).
- [22] A. Kardakova, M. Finkel, D. Morozov, V. Kovalyuk, P. An, C. Dunscombe, M. Tarkhov, P. Mauskopf, T. Klapwijk, and G. Goltsman, The electron-phonon relaxation time in thin superconducting titanium nitride films, *Appl. Phys. Lett.* **103**, 252602 (2013).
- [23] Y. Xu, W. Fu, Y. Zhou, M. Xu, M. Shen, A. A. Sayem, and H. X. Tang, Light-induced dynamic frequency shifting of microwave photons in a superconducting electro-optic converter, *Phys. Rev. Appl.* **18**, 064045 (2022).
- [24] L. Fan, C.-L. Zou, R. Cheng, X. Guo, X. Han, Z. Gong, S. Wang, and H. X. Tang, Superconducting cavity electro-optics: A platform for coherent photon conversion between superconducting and photonic circuits, *Sci. Adv.* **4**, eaar4994 (2018).
- [25] Y. Xu, Ph.D. thesis, School of Engineering and Applied Science, Yale University, 2022.
- [26] J. R. Lane, D. Tan, N. R. Beysengulov, K. Nasyedkin, E. Brook, L. Zhang, T. Stefanski, H. Byeon, K. W. Murch, and J. Pollanen, Integrating superfluids with superconducting qubit systems, *Phys. Rev. A* **101**, 012336 (2020).
- [27] G. Koolstra, G. Yang, and D. I. Schuster, Coupling a single electron on superfluid helium to a superconducting resonator, *Nat. Commun.* **10**, 5323 (2019).
- [28] N. Samkharadze, A. Kumar, M. J. Manfra, L. Pfeiffer, K. West, and G. Csáthy, Integrated electronic transport and thermometry at millikelvin temperatures and in strong magnetic fields, *Rev. Sci. Instrum.* **82**, 053902 (2011).